JOURNAL OF THE AMERICAN CHEMICAL SOCIETY

pubs.acs.org/JACS

Article

Machine Learning-Accelerated Discovery of A_2BC_2 Ternary Electrides with Diverse Anionic Electron Densities

Zhiqi Wang, Yutong Gong, Matthew L. Evans, Yujing Yan, Shiyao Wang, Nanxi Miao, Ruiheng Zheng, Gian-Marco Rignanese, and Junjie Wang*

Cite This: *J. Am. Chem. Soc.* 2023, 145, 26412−26424

Read Online

ACCESS | Metrics & More | Article Recommendations | Supporting Information

Downloaded via UNIV CATHOLIQUE DE LOUVAIN on January 19, 2024 at 09:58:29 (UTC).
See https://pubs.acs.org/sharingguidelines for options on how to legitimately share published articles.

ABSTRACT: This study combines machine learning (ML) and high-throughput calculations to uncover new ternary electrides in the A_2BC_2 family of compounds with the *P4*/*mbm* space group. Starting from a library of 214 known A_2BC_2 phases, density functional theory calculations were used to compute the maximum value of the electron localization function, indicating that 42 are potential electrides. A model was then trained on this data set and used to predict the electride behavior of 14,437 hypothetical compounds generated by structural prototyping. Then, the stability and electride features of the 1254 electride candidates predicted by the model were carefully checked by high-throughput calculations. Through this tiered approach, 41 stable and 104 metastable new A_2BC_2 electrides were predicted. Interestingly, all three kinds of electrides, i.e., electron-deficient, electron-neutral, and electron-rich electrides, are present in the set of predicted compounds. Three of the most promising new electrides (two electron-rich, Nd_2ScSi_2 and La_2YbGe_2, and one electron-deficient Y_2LiSi_2) were then successfully synthesized and characterized experimentally. Furthermore, the synthesized electrides were found to exhibit high catalytic activities for NH_3 synthesis under mild conditions when Ru-loaded. The electron-deficient Y_2LiSi_2, in particular, was seen to exhibit a good balance of catalytic activity and chemical stability, suggesting its future application in catalysis.

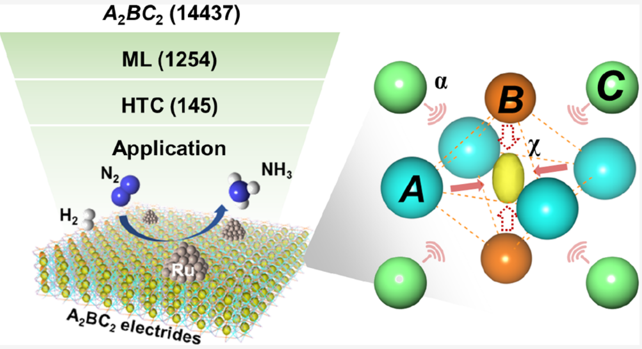

INTRODUCTION

Electrides[1−3] are a particular class of materials in which the excess valence electrons localize within interstitial cavities where they behave as anions. Since these localized electrons are no longer bound to any nucleus, they are typically reported to occupy energy bands close to the Fermi level.[1] As a result, electrides generally exhibit a low work function. Since the successful synthesis of the first stable inorganic electride $[Ca_{24}Al_{28}O_{64}]^{4+}(e^-)_4$ (C12A7:e^-),[2] electride materials have attracted widespread interest for a variety of applications, including organic light-emitting diodes (OLEDs),[4] superconductors,[5] battery anodes,[6] and catalysts[7−12] for ammonia (NH_3) synthesis and CO_2 reduction.

Considering the limited number of known electrides and their immense potential, discovering new stable electrides is an important task. Previously, the identification of new electrides relied on detailed experiments, from synthesis up to characterization, with compound selection being guided by intuition and chemical design rules.[13−15] Presently, new opportunities to accelerate the discovery of electrides are provided by high-throughput (HT) *ab initio* computations with two possible approaches. The first one is to screen for electrides within material databases of previously synthesized phases.[16−20] Various useful descriptors have been previously used to perform such differentiation between electrides and non-electrides. For example, Dale and Johnson suggested the electron localization function (ELF) and localized-orbital locator (LOL) as the most reliable descriptors for organic, inorganic, 2D, elemental, and molecular electrides.[21] Based on the electrostatic and electronic analyses of Ca_2N, Sr_2N, and Ba_2N, Walsh and Scanlon proposed to use the electrostatic potential to identify the localized nature of excess electrons of 2D electrides.[22] Although this screening method can highly accelerate the pace of electride identification, new electrides are limited to materials already existing in the databases. The second approach is to design electrides with completely new structures using structure prediction algorithms.[23−26] In contrast to computational screening, structure prediction may yield unexpected discoveries beyond the content of the material databases. However, it would be too demanding to use the characteristics of electrides as the target for a global

Received: September 24, 2023
Revised: November 2, 2023
Accepted: November 6, 2023
Published: November 21, 2023

© 2023 American Chemical Society

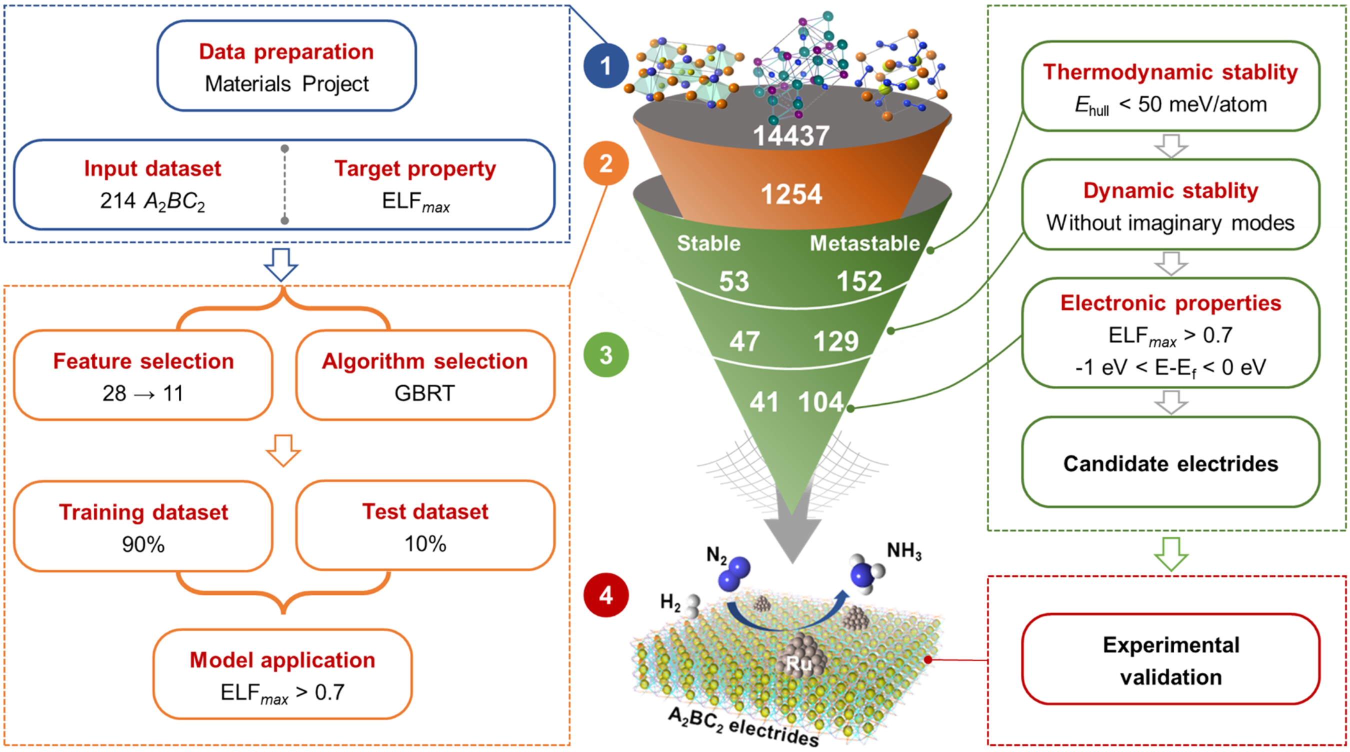

Figure 1. Illustration of our search framework for new ternary electrides by combining ML and HT computation. The dashed blue box describes the establishment of the *input data set* from available A_2BC_2 data. The dashed orange box represents the material screening process based on the ML results. The dashed green box corresponds to the stability evaluation and the DFT calculation of the electronic properties of the selected candidates. Finally, the red box shows experimental verification of the predictions.

structure search without any restrictions on possible compositions. In fact, previous successful attempts at electride discovery[18−20] were limited to electron-rich compositions. Since then, the search space for electrides has dramatically expanded. For example, ternary intermetallic electrides have attracted considerable attention due to their excellent chemical stability and catalytic performance.[9,27] Moreover, electron-neutral and -deficient electrides have also been proposed recently.[28,29] These extensions of the chemical space make this approach prohibitively time-consuming when relying only on *ab initio* calculations.

In recent years, machine learning (ML) has been successfully applied in many fields of materials research, such as the design of crystal structures,[30−32] the development of interatomic potentials,[33,34] and the prediction of material properties.[33−36] In particular, ML-based searches for new materials that meet specific requirements in a huge chemical space have proved effective for different material systems.[35,37−42] Compared to HT *ab initio* computations, ML subverts the need for exhaustive quantum mechanical calculations, rendering combinatorial chemical spaces tractable. In turn, ML can provide insights into the complex relationships between composition and properties.[43−45] However, this approach requires a sufficiently large training data set (consisting of both electrides and non-electride compounds) to obtain a reasonable surrogate model.

In this work, ML and HT *ab initio* computational screening are combined to discover electrides among ternary compounds with the structural prototype A_2BC_2 (space group $P4/mbm$, No. 127). Indeed, when considering all possible binary and ternary compounds available in existing databases, the A_2BC_2 prototype shows the highest number of known electrides, increasing the chances of achieving a predictive ML model in this region. Furthermore, this prototype covers a significant search space with ∼14,500 possible compounds (see below). By screening among these, 44 stable and 115 metastable A_2BC_2 ternary electrides with diverse anionic electron densities were identified computationally. Moreover, some of our predicted results were verified experimentally: two new electron-rich (Nd_2ScSi_2 and La_2YbGe_2) and one electron-deficient (Y_2LiSi_2) ternary electrides were successfully synthesized and studied as catalysts for NH_3 synthesis.

■ RESULTS AND DISCUSSION

Screening Framework for Ternary Electrides. The designed framework to screen new ternary electrides by combining HT calculations and ML is illustrated in Figure 1. First, 214 A_2BC_2 compounds with space group $P4/mbm$ were identified in the Materials Project (MP) database.[46] First-principles calculations were then performed for these 214 compounds, allowing us to identify 42 structures as electrides (listed in Table S1 excluding the 13 electrides reported by Zhu et al.[17]). To this end, we used the ELF[47] value at the center of the octahedral void of the A_2BC_2 structure (referred to as ELF_{max} hereafter) as a proxy (see discussion below). The ELF value is a measure of the likelihood of finding an electron with the same spin as a reference electron at a given point in the neighboring space. It quantifies the degree of spatial localization of the reference electron. Then, the calculated ELF_{max} of the 214 A_2BC_2 structures, including electrides and non-electrides, were used as the training set for a variety of ML models, as illustrated in the left panel of Figure 1. Several combinations of feature selection, algorithm selection, and model training regimes were systematically explored to

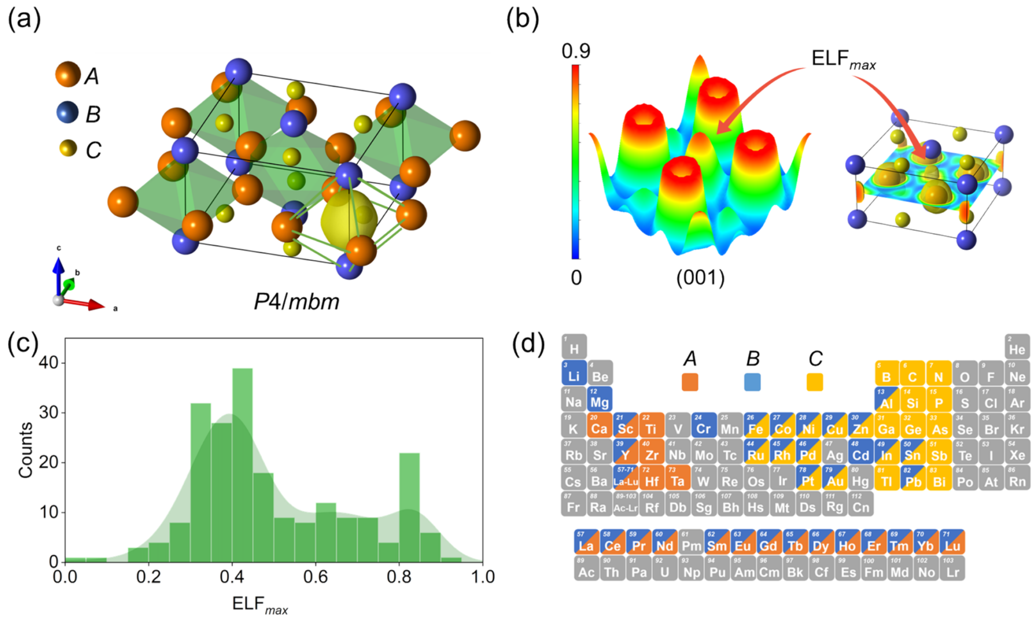

Figure 2. Preparation of the *input data set* used for training the ML model. (a) Structure and calculated electron localization function (ELF) for an example (Yb_2MgP_2) of A_2BC_2 ($P4/mbm$, No. 127) compounds. (b) Location of the target value ELF_{max} in the structure. (c) ELF_{max} distribution for the 214 existing A_2BC_2 compounds in Materials Project database. (d) Illustration of the chemical elements considered to build the *prediction data set* of A_2BC_2 compounds.

determine the optimal model. Next, the optimal trained ML model was applied to predict the electride properties of hypothetical A_2BC_2 phases. After that, HT density functional theory (DFT) calculations were performed to study the thermodynamic and chemical stabilities of the most promising electride candidates suggested by the ML model (right panel of Figure 1). Finally, experiments were conducted to synthesize the predicted new ternary electrides to verify the theoretical predictions.

This approach is workable only if there exists a figure of merit for the target property that is readily computable by DFT. ELF calculations have been the most widely used tool for analyzing electrides,[17−20,48] and the resulting predictions have been found to agree well with experimental observations.[49] Typically, electrides exhibit a maximum in the ELF at the interstitial position with a value of 0.75 or greater.[50−52] There are, however, a few exceptions, such as C12A7:e^-, which was reported to have a small ELF value of around 0.45. It is a nonstoichiometric electride with only one-third of electrons localized in a cage.[47] In this study, ELF calculations were performed for 214 A_2BC_2 compounds gathered from the MP (Table S2). We identified 42 potential electrides in which the electrons typically localize at the highly symmetrical octahedral voids surrounded by A and B atoms. Figure 2a,b shows the ELF_{max} values of Yb_2MgP_2 as an example. The bimodal distribution of the ELF_{max} values for the 214 A_2BC_2 compounds is displayed in Figure 2c. It presents a significant peak at around 0.8, which is typical of the potential electrides. Consequently, we decided to use the ELF_{max} value as a proxy to determine whether a material is potentially an electride and then to build an ML model with ELF_{max} as the target value. Considering the estimated uncertainty in the ML predictions, the screening criterion for possible electrides was slightly relaxed to $ELF_{max} > 0.7$.

The *input data set* was obtained by gathering the compositions and calculated ELF_{max} values of the 214 existing A_2BC_2 compounds. It was then randomly split into training and test sets with 90 and 10% of the data, respectively.

The *prediction data set* was constructed through a simple element replacement strategy without considering charge balance. By selecting elements from existing A_2BC_2 compounds (i.e., 21, 29, and 25 candidate elements for A, B, and C sites, respectively (Figure 2d)), 15,225 compounds were generated. After excluding those already present in the input data set, the prediction data set contains 14,437 ternary A_2BC_2 compounds.

Algorithm and Feature Selection. Besides the *input data set* itself, the identification of the most relevant features and of an appropriate algorithm can greatly enhance generalization and accuracy.

In fact, the algorithm and features are quite strongly intertwined. On the one hand, the choice of relevant features is crucial for the ML model to achieve good prediction performance. On the other hand, the accuracy of the ML model can be used as an indicator to validate the selected features. Since our target value is the interstitial electronic characteristic (ELF_{max}) of the A_2BC_2 compounds, we considered features related to the structure and various atomic properties that can significantly affect ELF_{max}. In total, 28 input features were considered including the first ionization energy and the atomic radii of the selected elements as well as the electronegativity difference between them. The complete list of these input features can be found in Table S3. By selecting the intrinsic properties of elements as features, no additional DFT calculations are required in the featurization process, which enables the screening of much larger chemical spaces.

For the ML model, we assessed five regression algorithms that have been widely used for predicting material properties: Decision Tree Regressor (DTR),[53] Adaptive Boosting Regressor (ABR),[54] eXtreme Gradient Boosting Regressor (XGBR),[55] Support Vector Regression (SVR),[56] and Gradient-Boosted Regression Tree (GBRT).[57] They were compared based on the root mean squared error (RMSE) and the

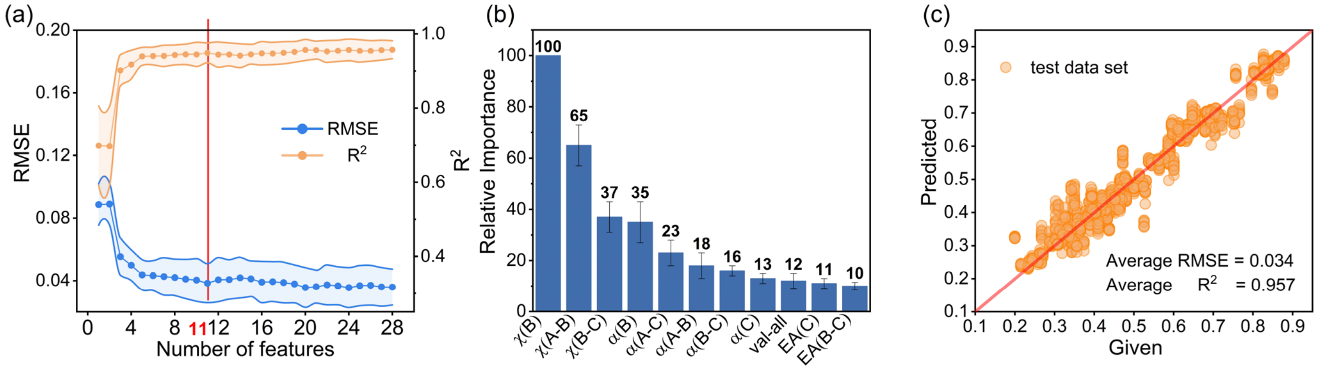

Figure 3. Training and performance of the machine learning model. (a) Extraction of important features by the wrapper method. (b) Calculated feature importance for the $\mathrm{ELF_{max}}$ value of A_2BC_2 compounds based on GBRT. (c) Prediction of the $\mathrm{ELF_{max}}$ values for the test set of the A_2BC_2 compounds.

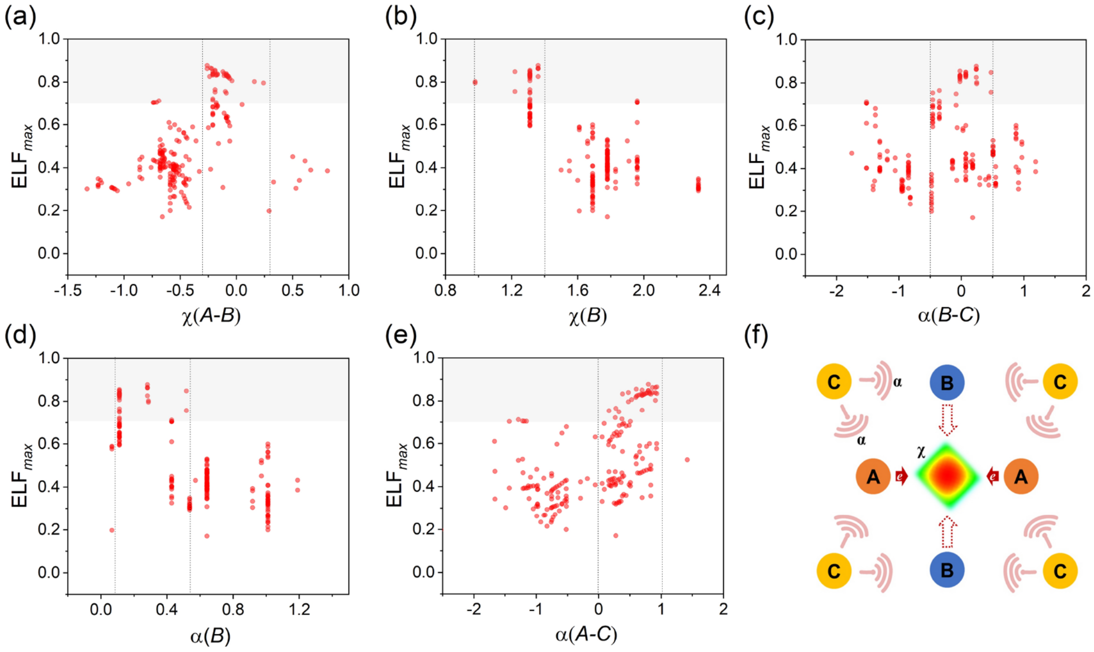

Figure 4. Analysis of interstitial electron formation in A_2BC_2 electrides. Distribution of $\mathrm{ELF_{max}}$ in the training data set as functions of five features of (a) $\chi(A-B)$, (b) $\chi(B)$, (c) $\alpha(B-C)$, (d) $\alpha(B)$, and (e) $\alpha(A-C)$. (f) Schematic diagram of the interstitial electron formation.

determination coefficient (R^2) (Figure S1a). To optimize the hyperparameters of each model, a fivefold cross-validation was performed on the training set (90% of the input data set), and each final model was evaluated on the same test set. It can be seen from Figure S1a that all five algorithm models perform well, with the GBRT algorithm yielding the highest accuracy; thus, it was chosen to build the follow-up ML models.

To limit the dimensions, a model-based wrapper method was used for the feature selection. The feature importance score obtained from the GBRT algorithm was used to remove features iteratively, with an ML model trained at each step using the remaining features. This process was repeated, until only one feature remained. For reliability, the importance score of each feature at each step was obtained as the average of 10 training runs (Table S4). The feature selection process is illustrated in Figure 3a. The best results (the global extremum in the RMSE and R^2 indicators) are achieved with 20 features, but using only 5 or 11 of them (which are local extrema in RMSE and R^2 indicators) already lead to sufficiently predictive results (the R^2 indicator decreases only by 2 and 1%, respectively). To ease the interpretability of the model while maintaining a high accuracy, we decided to work with 11 features (as listed in Table S3). After conducting 100 random tests, the average importance scores of these 11 features (Figure 3b) exceeded 10. Next, the test set was used to evaluate the generalization ability and accuracy of the trained model. The RMSE and R^2 indicators were obtained by averaging over 100 tests (Figure 3c), and the results were 0.034 and 0.957, respectively. This demonstrates that the trained ML model has a performance sufficient to screen electride properties of the unseen hypothetical materials and reduce the number of required calculations.

Since our aim is to identify phases with $\mathrm{ELF_{max}} > 0.7$, we utilized the algorithm in a classification context in order to validate the model's ability to accurately classify the ELF value. The confusion matrix (Figure S1b) of the classification demonstrates a high level of accuracy (0.94), indicating that the model can reliably identify phases with an $\mathrm{ELF_{max}} > 0.7$.

Analysis of Interstitial Electron Formation Based on ML Results. Although the ML model trained in this study used 11 features, it is evident from the feature importance in Figure 3b that the top five features (which correspond to a local extremum in the RMSE and R^2 indicators, see discussion above) have a considerable impact on the performance of the model (importance score >20). These mainly consist of the electronegativity, χ, and polarizability, α, of the constituent atoms. Meanwhile, the corresponding values for RMSE and R^2 using these five features are 0.044 and 0.940, respectively. These suggest that these five features play a crucial role in determining the formation of interstitial electrons. In the following analysis, the reasons behind the significant influence of these features on the formation of interstitial electrons were examined.

The distribution of the values of the five features, $\chi(B)$, $\chi(A-B)$, $\alpha(B-C)$, $\alpha(B)$, and $\alpha(A-C)$, in the training data is shown in Figure 4a−e. These features can be divided into two parts based on the competition for electrons among different atoms. The first part ($\chi(A-B)$ and $\chi(B)$) describes the relationship between atoms A and B, while the second part ($\alpha(B-C)$, $\alpha(B)$, and $\alpha(A-C)$) focuses on the features about A (B) and C atoms.

$\chi(A-B)$ and $\chi(B)$ describe the influence of the competition between atoms A and B on the formation of interstitial electrons. The atoms influencing these two features are precisely those constituting the octahedron that surrounds the interstitial electrons. As shown in Figure 4a and b, $\mathrm{ELF}_{\max}$ values around 0.8 correspond to values of $\chi(A-B)$ between -0.3 and 0.3 and values of $\chi(B)$ ranging from 1 to 1.4, respectively. Figure 4a shows that as the electronegativity difference $\chi(A-B)$ increases from -1.5 to 0, the $\mathrm{ELF}_{\max}$ of the interstitial electrons also increases. Furthermore, the distribution of $\mathrm{ELF}_{\max}$, as shown in Figure 4b, exhibits a strong correlation with the electronegativity of the B atom. It is revealed that the comparable electronegativities of A and B atoms favor the formation of interstitial electrons of electrides.[17]

For further insight into the formation of interstitial electrons, the electronic structures of a series of Y_2BSi_2 compounds (B = Li, Mg, Sc, and Al with χ of 0.98, 1.31, 1.36, and 1.60, respectively; $\chi(Y)$=1.22) were calculated as an example and are shown in Figure S2. By analyzing the atomic and interstitial electrons projected band structures (Figure S2a−c), we found that interstitial electrons are mainly contributed by Y atoms when the values of $\chi(B)$ are 0.98, 1.31, and 1.36. This is consistent with the ML result that interstitial electrons can be formed only when the $\chi(A-B)$ value is within the range of -0.3 to 0.3 (Figure 4a). When $\chi(B)$ is too large ($\chi(\mathrm{Al})$=1.6), the interstitial electrons will be captured by the B atom, resulting in the formation of a multicenter bonding instead of interstitial electrons (Figure S2d). The variation of calculated $\mathrm{ELF}_{\max}$ of Y_2BSi_2 compounds as a function of $\chi(A-B)$ or $\chi(B)$ is shown in Figure S3a,b. Since the electronegativity is the measure of the ability of atoms to attract electrons in compounds, a possible interpretation is that the interstitial electrons in the octahedron are donated by A atoms and are stabilized due to the competition between the A and B atoms.

Based on the above analysis, it can be inferred that electronegativities of cations A and B have a direct impact on the formation of interstitial electrons, which is consistent with the mechanism proposed in previous research.[17] However, our ML analysis further revealed that the polarizability of the cations and anions has a significant influence on the strength of interstitial electrons. Table S4 shows that the values of RMSE and R^2 using the two features $\chi(A-B)$ and $\chi(B)$ are 0.089 and 0.698, respectively. After considering the next three features $\alpha(B-C)$, $\alpha(B)$, and $\alpha(A-C)$, the quality of the trained model is significantly improved, with RMSE and R^2 values of 0.044 and 0.940, respectively, which are very close to those (0.038 and 0.949) by using 11 features.

The polarizability of an atom represents the degree to which the valence electrons deform when the atom is subjected to an electric field. The calculated $\mathrm{ELF}_{\max}$ as a function of $\alpha(B-C)$ is shown in Figure 4c. It can be observed that $\alpha(B-C)$ values corresponding to high $\mathrm{ELF}_{\max}$ values are near zero (Figure 4c). In contrast, the values of $\alpha(A-C)$ mostly lie between 0 and 1 when interstitial electrons exhibit a high degree of localization. It has been revealed that electropotential wells can be formed at interstitial sites of electrides to accommodate electrons.[16] Therefore, one can conclude that a high polarizability of A atoms can favor the formation of electride electrons under an electrostatic potential in a crystal structure. Although the B atoms in A_2BC_2 electrides have electronegativities comparable to those of the A atoms, for the emergence of electrides, it is highly likely that the B atoms have a low polarizability comparable to that of the C atoms, as shown in Figure 4c,e.

The calculated $\mathrm{ELF}_{\max}$ of Y_2ScC_2 (C = Pb, Ga, In, and Tl) compounds as a function of $\alpha(B-C)$ illustrates the influence of relative polarizability (Figure S3c). When the electronegativity difference between Y (A atom) and Sc (B atom) satisfies the electronegativity condition ($\chi(A-B) = -0.14$), the degree of localization of interstitial electrons increases first with the polarization difference ($\alpha(B-C)$) and then decreases. This result illustrates that when the polarizability of B cations is slightly greater than that of the C anions, the localization of interstitial electrons is robust. With the further increase of B polarizability, the valence electrons of B atoms can be attracted by C atoms instead of forming anionic electrons at interstitial sites. This indicates that the polarizability of C atoms can indirectly affect the spatial distribution of the valence electrons of the B atom through the polarizability difference between C and B atoms and then affect the formation of interstitial electrons of electrides. Furthermore, the calculated $\mathrm{ELF}_{\max}$ of Y_2BSi_2 (B = Mg, Ca, Sr, and Ba) as a function of $\alpha(B)$ and the calculated $\mathrm{ELF}_{\max}$ of Y_2MgC_2 (C = Al, Ga, In, and Tl) as a function of $\alpha(A-C)$ are shown in Figure S3d and e, respectively. In summary, the degree of localization of interstitial electrons is greater and the polarizability of B atoms is lower and comparable to that of C atoms.

To better understand the formation of interstitial electrons in A_2BC_2 and the synergy of electronegativity and polarizability, a schematic diagram is drawn as shown in Figure 4f. The following picture emerges from the interpretation of the ML model from this work: although A and B atoms have similar electronegativity, due to the greater polarizability of the A atom, the valence electrons of A atoms migrate to the interstitial position under the action of the electrostatic field in the crystal while the valence electrons of B atoms are transferred to the C atoms to balance the charge distribution inside of the A_2BC_2 compound.

Therefore, it can be concluded from the feature extraction based on ML training that A and B atoms have a direct influence on the formation of interstitial electrons, while C atoms influence the emergence of electrons through an indirect but significant effect of relative polarizability, which was not mentioned in previous studies. This shows that ML can help us

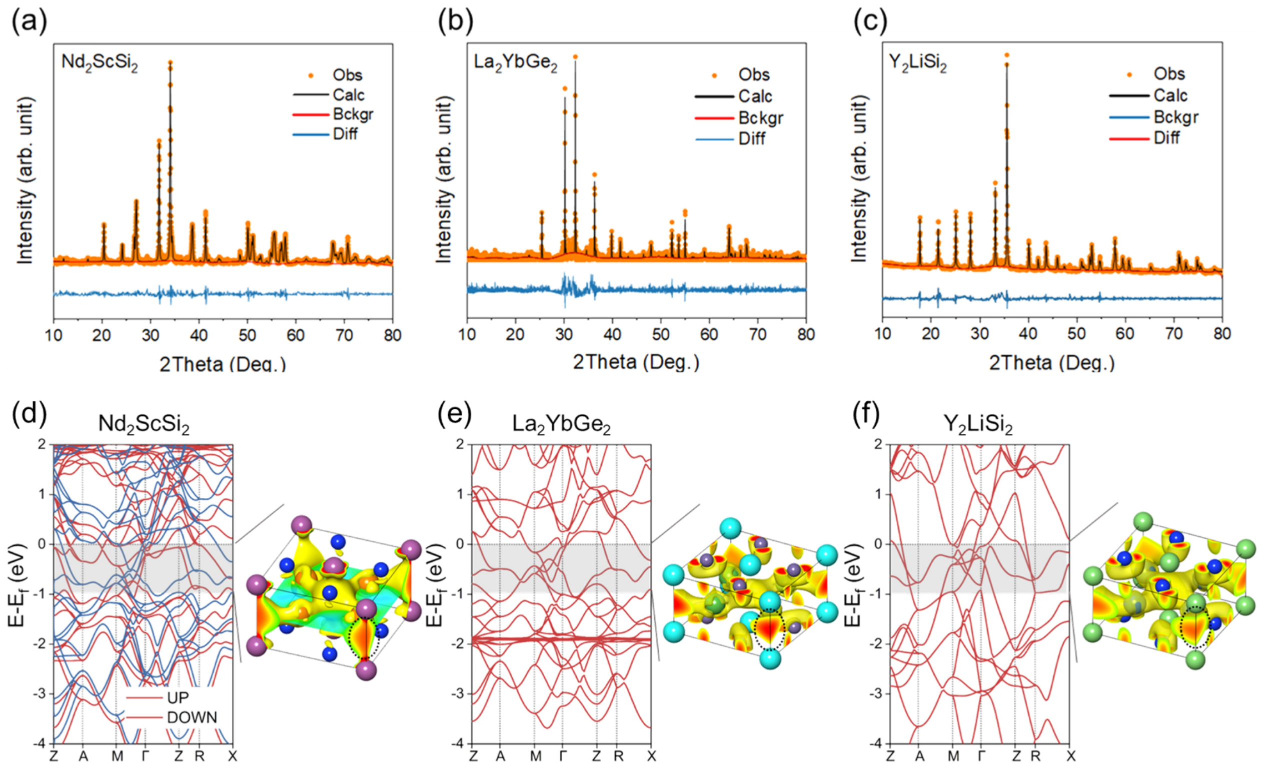

Figure 5. Crystal and electronic structures of predicted A_2BC_2 electrides. XRD patterns with Rietveld refinement of Nd_2ScSi_2 (a), La_2YbGe_2 (b), and Y_2LiSi_2 (c). Calculated electronic structures of Nd_2ScSi_2 (a), La_2YbGe_2 (b), and Y_2LiSi_2 (c).

better understand the formation of interstitial electrons in A_2BC_2 compounds, allowing us to devise increasingly complex chemical design rules. Although the above mechanism obtained with the help of ML is based only on the A_2BC_2 prototype, it may help us understand, design, and discover new electrides with other structural prototypes.

Electride Prediction by the ML Model and High-Precision DFT Calculations. Using the predictions of our well-trained ML model, the 14,437 constructed A_2BC_2 compounds were screened with the prediction criterion of $\mathrm{ELF_{max}} > 0.7$. As displayed in Figure 1, 1254 compounds were predicted by the model to be candidate electrides.

To assess their synthesizability, the thermodynamic and dynamic stabilities of these 1254 candidate structures were further evaluated by further high-precision DFT calculations. Previous studies[17,18] have demonstrated that the calculated ELF alone is not enough to confirm the nature of electrides, as the localized electrons can occupy an energetic range far away from the Fermi level. Hence, a detailed electronic structure analysis is necessary for confirmation of the electride candidates.

To assess the thermodynamic stability of a given compound, the distance of its formation energy from the convex hull (E_{hull}) is a good indicator. Compounds with $E_{\mathrm{hull}} = 0$ are thermodynamically stable and have a high probability to be synthesizable. Therefore, we constructed ternary phase diagrams for the elements composing the 1254 electride candidates, considering the known competing phases reported in various databases.[46,58] Based on these calculations, 53 candidates were suggested to be thermodynamically stable. It is important to note that some thermodynamically metastable compounds can also be synthesized[59] and that the estimations from DFT may be inaccurate.[38] Therefore, we also considered all compounds with E_{hull} values lower than 50 meV/atom, generating a set of 152 thermodynamically metastable candidates.

Then, the dynamic stabilities of the 228 (53 + 152) candidate structures were investigated by phonon dispersion calculations. It turned out that 176 compounds were dynamically stable, as indicated by the lack of phonon modes with imaginary frequencies. Following this combination of thermodynamic and dynamic calculations, 47 stable and 129 metastable A_2BC_2 compounds are considered as potential electrides that can be synthesized.

A previous study[18] suggests that electrides should have the following characteristics: (1) the existence of localized interstitial electrons and (2) the energy level of the interstitial electrons is near the Fermi level. Consequently, high-accuracy DFT calculations of the electronic structure properties were performed for the 176 candidates. We analyzed electrons on the band structures and excluded the compounds for which the levels occupied by the interstitial electrons were outside of $-1\ \mathrm{eV} < E - E_F < 0$ eV energy window. Finally, 41 stable and 104 metastable A_2BC_2 structures were confirmed as potential electrides. The relaxed crystal structures and their computed properties have been deposited in the Materials Cloud Archive[60] (available at the DOI: 10.24435/materialscloud:c8-gy), which can be explored at https://electrides.modl-uclouvain.org via the web UI and programmatic OPTIMADE API.[61,62]

Electrides have long been thought to only exist in electron-rich systems.[2] Very recently, it was demonstrated that electrides can be electron-neutral[63] or even electron-deficient[28,64] compounds. As the elements in A_2BC_2 compounds have variable valence states, it is expected that different types of electrides, i.e., electron-rich, -neutral, and -deficient electrides, can be found in this A_2BC_2 material family. Indeed, such an expectation was confirmed by the electronic structure calculations for the screened 187 new electrides. For instance, the highest valence state of yttrium (Y) is +3 and the valence state of silicon (Si) as an anion can be −4. When Y and Si were used as A and C elements, respectively, the charge balance conditions of A_2BC_2 electrides could be tuned by choosing different B elements with different valence states. It is well known that lithium (Li), magnesium (Mg), and scandium (Sc) are +1, +2, and +3, respectively. Therefore, the candidates Y_2LiSi_2, Y_2MgSi_2, and Y_2ScSi_2 predicted in this work can be electron-deficient, -neutral, and -rich electrides, respectively (Figure S2a−c). In total, 13 electron-deficient electrides, Y_2LiSi_2, Sc_2LiSi_2, La_2LiSi_2, Ce_2LiSi_2, Pr_2LiSi_2, Sm_2LiSi_2, Tb_2LiSi_2, Dy2LiSi2, Ho_2LiSi_2, Er_2LiSi_2, Tm_2LiSi_2, Lu_2LiSi_2, and La_2LiGe_2, were identified to be synthesizable at ambient pressure by high-precision DFT calculations. This result proves that the electron-rich condition of the compound can be relaxed for future studies screening electrides.[63]

Among the final candidates, it is worth highlighting 7 stable and 29 metastable A_2BC_2 electrides, e.g., Yb_2LiP_2 and Ce_2LiSi_2, presenting magnetism. Table S5 shows the complete list of A_2BC_2 electrides with magnetic properties. Their specific magnetic properties still need to be studied further with more accurate computational approaches. Hence, they are not discussed in detail here. However, it is worth mentioning that the magnetic properties of Ce_2MgSi_2 have already been studied in a previous work,[65] but its electride nature had not been noticed.

Experimental Validation of Predicted Electrides. Based on the prediction results, two new electron-rich (Nd_2ScSi_2 and La_2YbGe_2) electrides and one electron-deficient (Y_2LiSi_2) A_2BC_2 electride were successfully synthesized, the La_2YbGe_2 for the first time. While Nd_2ScSi_2[66] and Y_2LiSi_2[67] have been previously reported outside of the context of electrides, we believe this is the first report of La_2YbGe_2. We conducted Rietveld refinements of the X-ray diffraction pattern using the predicted structures of the three newly synthesized electrides. Figure 5a−c shows that the simulated peak (black) positions have an excellent correlation with the experimental pattern (orange). Additionally, the difference plot (blue) indicates an acceptable fit with the refined profile and calculated unit-cell parameters for all three structures. Their calculated electronic structures are also shown in Figure 5d−f. The energy levels of interstitial electrons of the three electrides are close to the corresponding Fermi levels, which is a typical characteristic of electrides. Due to the presence of d electrons from transition metals and f electrons from rare earth elements in Nd_2ScSi_2, La_2YbGe_2, and Y_2LiSi_2, the strong on-site Coulomb correlation effects were taken into consideration using the DFT + U approach. As a result, it was verified that Nd_2ScSi_2 is a magnetic electride whereas La_2YbGe_2 and Y_2LiSi_2 exhibit nonmagnetic properties. Although electron-deficient electrides have already been predicted theoretically at high pressure,[28,64] Y_2LiSi_2 is the first confirmed electron-deficient electride at atmospheric pressure, hence expanding the chemical space of electrides.

The ability for reversible hydrogen storage and low work function are two important characteristics of electrides in experiments.[68,69] Therefore, we conducted these two characterizations on three new electrides.

At low temperature (<200 °C), the anionic electrons in electrides present a high affinity for H atoms while, at higher temperatures, the trapped hydrogen can be released. This reversible storage ability can be beneficial for NH_3 synthesis by alleviating hydrogen poisoning of Ru catalysts.[7] This capability was confirmed for the three new proposed electrides. Our samples can be easily hydrogenated under a H_2 atmosphere at 200 °C, and the H release takes place for temperatures ranging from 300 to 500 °C: the hydrogen temperature-programmed desorption (H_2-TPD) measurements show hydrogen desorption peaks at 499, 349, and 391 °C for Nd_2ScSi_2, La_2YbGe_2, and Y_2LiSi_2, respectively (Figure 6a). This result is in very nice agreement with the DFT-calculated desorption energies (Figure 6b), which are 1.58, 0.71, and 1.14 eV for Nd_2ScSi_2, La_2YbGe_2, and Y_2LiSi_2, respectively. Note also that our DFT simulations show that the trapped H atom sits where the anionic electrons were prior to hydrogenation, and the corresponding electronic states are moved away from the Fermi level to lower energies (Figure S4). Coming back to the result of experimental H_2-TPD measurements (Figure 6a), the desorption peaks at higher temperatures (725, 695, and 618 °C for Nd_2ScSi_2, La_2YbGe_2, and Y_2LiSi_2, respectively) can be attributed to the dynamics of the escape process of the H atom from the bulk. Therefore, both our experimental and computational results reveal a good H adsorption−desorption ability for Nd_2ScSi_2, La_2YbGe_2, and Y_2LiSi_2 in the 300−500 °C temperature range, making these three new electrides potential candidates to solve the hydrogen poisoning problems during catalytic NH_3 synthesis, which arises from the strong adsorption of hydrogen on the metal surface.[70,71]

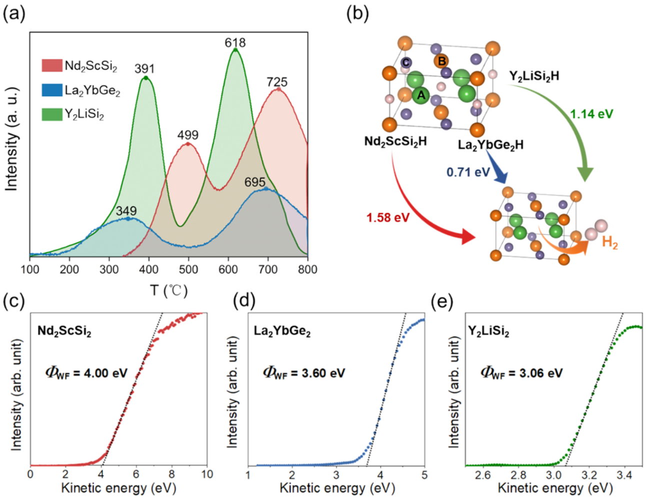

Figure 6. Hydrogen storage properties and measured work functions of Nd_2ScSi_2, La_2YbGe_2, and Y_2LiSi_2. (a) H_2 TPD spectra of hydrogenated of three new electrides. (b) Energy change of hydrogen desorption for three electrides at 0 K obtained by DFT calculations. (c−e) The measured work functions of the three electrides by UPS (He, $h\nu$ = 21.2 eV).

Using ultraviolet photoelectron spectroscopy (UPS), the work functions (Φ_{WF}) of Nd_2ScSi_2, La_2YbGe_2, and Y_2LiSi_2 were measured to be 4.0, 3.6, and 3.06 eV, respectively, from the cutoff energy of the secondary electrons (Figure 6c−e). The corresponding DFT values were computed to be 2.75−3.8 eV (Nd_2ScSi_2), 2.45−3.17 eV (La_2YbGe_2), and 2.86−3.7 eV (Y_2LiSi_2) (Figure S5). Given the approximations involved, these calculated values can be considered as qualitatively consistent with the experimental measurements. These low work functions suggest the potential for efficient electron donation, thereby promoting N_2 activation when electrides are utilized as catalyst supports for Ru.[9,66]

Motivated by their great potential for NH_3 synthesis, we synthesized Ru-loaded Nd_2ScSi_2, La_2YbGe_2, and Y_2LiSi_2 and evaluated their catalytic performances. The loading amounts in our experiments were set as 2 and 5% (weight percent). The actual loading amounts of Ru measured by inductively coupled plasma (ICP) method on Nd_2ScSi_2 are 1.4 and 3 wt %, while those on La_2YbGe_2 are 1.4 and 2.8 wt %. Interestingly, it was found that the loading of Ru of electron-deficient electride Y_2LiSi_2 is much easier than those on Nd_2ScSi_2 and La_2YbGe_2. The measured loading amounts on Y_2LiSi_2 are 1.9 and 4.9 wt %, which are almost identical with the values for nominal loading. The catalytic performance of the electron-rich A_2BC_2 electrides is shown in Figure 7a (where x%Ru/A_2BC_2 denotes A_2BC_2 loaded with x wt % Ru) in comparison with those of traditional oxide-supporting catalysts and of other reported electride-supporting catalysts. One can see that the catalytic activities of 3%Ru/Nd_2ScSi_2 (2800 μmol g_{cat}^{-1} h^{-1}) and 1.4%Ru/Nd_2ScSi_2 (3000 μmol g_{cat}^{-1} h^{-1}) are much higher than those previously reported[11] at 400 °C and 0.1 MPa. The NH_3 synthesis activities of 1.4%Ru/La_2YbGe_2 (1250 μmol g_{cat}^{-1} h^{-1}) and 2.8%Ru/La_2YbGe_2 (1150 μmol g_{cat}^{-1} h^{-1}) are higher than that of 2%Ru/Y_5Si_3 (800 μmol g_{cat}^{-1} h^{-1}), the first intermetallic electride catalyst. Interestingly, it should be noted that the catalytic activities of these two new electrides are not sensitive to the Ru loaded. This can most probably be attributed to the fact that all A_2BC_2 electrides synthesized in this work display very small specific areas (<1 m^2/g). As derived from the Arrhenius plots, the apparent activation energy (E_a) for the NH_3 synthesis of 3%Ru/Nd_2ScSi_2 is 42 kJ mol^{-1} (Figure 7b), which is lower than those of conventional Fe-based and Ru-based catalysts and is comparable to those reported for other electride-based catalysts.[7,70,71] The NH_3 synthesis activity of 3%Ru/Nd_2ScSi_2 shows a monotonic increase with the pressure, reaching 8300 μmol g_{cat}^{-1} h^{-1} at 1 MPa (Figure 7c). This is an important advantage of electrides in solving the problem of hydrogen poisoning. The stability of 3%Ru/Nd_2ScSi_2 was tested at 400 °C and 1 MPa (Figure 7d). The NH_3 synthesis activity remained stable at a value of ~2.5 mmol g_{cat}^{-1} h^{-1}, showing no obvious deactivation after a time-on-stream of 100 h.

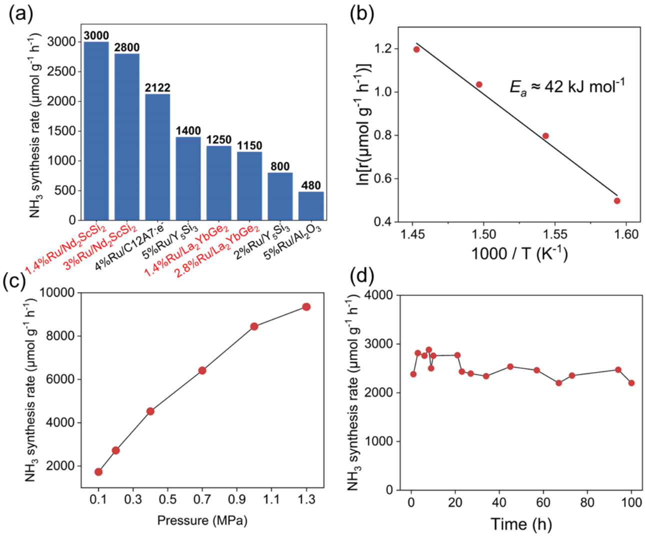

Figure 7. Performance evaluation of electron-rich A_2BC_2 electrides for NH_3 synthesis. (a) Activity comparison for different catalysts at 400 °C and 0.1 MPa. The data for 4%Ru/C12A7:e^- and 5%Ru/Y_5Si_3 are taken from the literature,[11] and the rest of the data is obtained on the same equipment. (b) Arrhenius plot of ammonia synthesis over Ru/Nd_2ScSi_2. (c) Activity of 3%Ru/Nd_2ScSi_2 at different reaction pressures. (d) Stability test of 3%Ru/Nd_2ScSi_2 within 100 h.

The catalytic activities of 4.9%Ru/Y_2LiSi_2 and 1.9%Ru/Y_2LiSi_2 catalysts are 2300 and 1800 μmol g_{cat}^{-1} h^{-1} (Figure 8a), respectively, which are comparable with the reported activities for the 4%Ru/C12A7:e^- and intermetallic electron-rich electride catalyst Ru/Y_5Si_3.[11] The E_a for the NH_3 synthesis on 4.9%Ru/Y_2LiSi_2 was calculated to be 65 kJ mol^{-1} (Figure 8b), which is higher than those of typical electron-rich electride catalysts but is still much lower than those of conventional Fe-based and Ru-based catalysts.[72,73] This indicates for the first time that electron-deficient electrides can act as an efficient support for the NH_3 synthesis. One main drawback of most reported electron-rich electrides, e.g., C12A7:e^- and Ca_2N,[74] is the lack of chemical stability in highly oxidative environments (e.g., in a water solution). Therefore, we assessed whether an electron-deficient electride could possess a superior stability. To this end, 0.5 g of the synthesized Y_2LiSi_2 sample was first washed with 40 mL of water and then centrifuged and lyophilized. By measuring its XRD pattern, it was found that the main phase is still Y_2LiSi_2 even after being submerged in water for 5 days (Figure S6). Then, using samples washed for 1 h and 5 days, two 4.9%Ru/Y_2LiSi_2 catalysts were synthesized and tested for NH_3 synthesis. Surprisingly, the NH_3 synthesis activities of 2000 μmol g_{cat}^{-1} h^{-1} (1 h) and 1600 μmol g_{cat}^{-1} h^{-1} (5 days) were still obtained (Figure 8a), demonstrating the durability of this electron-deficient electride in harsh environments, such as those of industrial NH_3 synthesis. It is noteworthy that the measured E_a of the catalyst using the Y_2LiSi_2 washed for 1 h is about 70 kJ mol^{-1} (Figure S7). This energy is much lower than that of reported Ru/Y_2O_3 (~100 kJ mol^{-1}),[75] which confirms that the Y_2LiSi_2 electride is still the active component after washing, rather than Y_2O_3.

The catalytic activity of 4.9%Ru/Y_2LiSi_2 was also measured as a function of pressure, as shown in Figure 8c. It increases monotonically with the pressure, reaching 8000 μmol g_{cat}^{-1} h^{-1} at 1 MPa, proving that this electron-deficient electride can also be used to circumvent the problem of hydrogen poisoning.

The catalytic activity of an electride-based catalyst is believed to be determined by the concentration of the anionic electrons. Namely, the stronger the localization of anionic electrons, the more active the electride-based catalyst. This belief stems from work by Hosono et al., who synthesized and studied the C12A7:e^- electride with different electron densities.[76] Nonetheless, there is so far no solid evidence to support this idea in other electrides due to the lack of materials on which it could be investigated. The A_2BC_2 electrides discovered in this work share the same crystal structure and possess different degrees of localized electrons at the interstitial sites and thus form the perfect playground to study the influence of the quantity of localized electrons on the performance of electride catalysts.

Various theoretical and experimental data were thus collected for the Nd_2ScSi_2, La_2YbGe_2, and Y_2LiSi_2 electrides. First, ELF calculations and Bader charge analysis were performed. The ELF_{max} of Y_2LiSi_2 (0.79) is found to be smaller than those of Nd_2ScSi_2 (0.85) and La_2YbGe_2 (0.88)

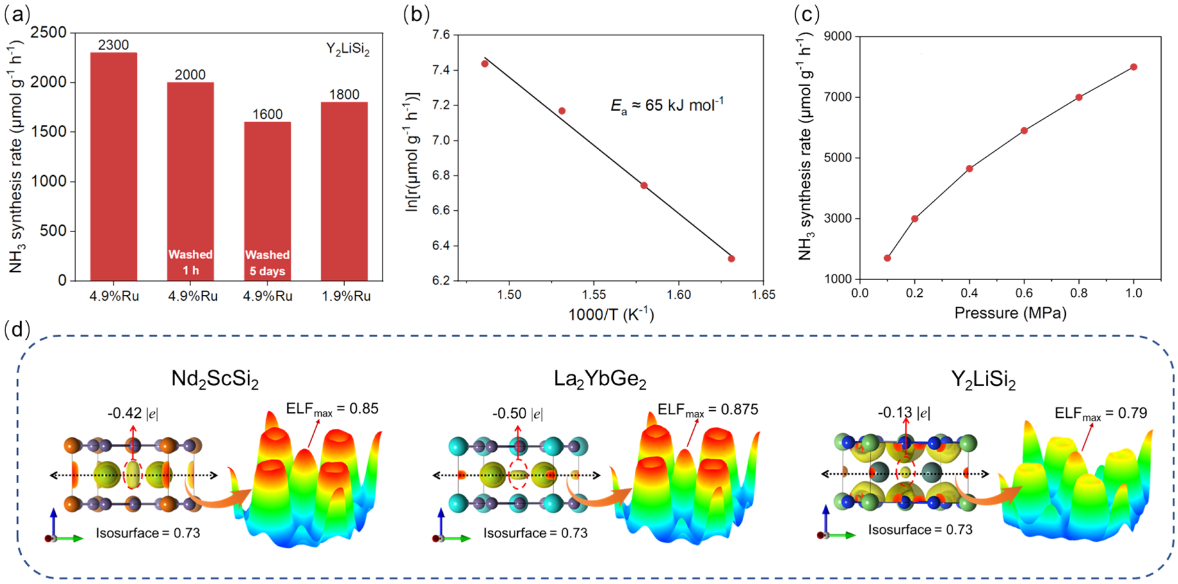

Figure 8. Catalytic ammonia synthesis performance and mechanism of electron-deficient electride Y_2LiSi_2. (a) Catalytic activities of Ru/Y_2LiSi_2. (b) Arrhenius plot of NH_3 synthesis over 4.9 wt % Ru-loaded as-synthesized Y_2LiSi_2. (c) Activity of 4.9 wt % Ru-loaded as-synthesized Y_2LiSi_2 under different pressures. (d) Calculated Bader charges and electron localization functions (ELF) of interstitial electrons of Nd_2ScSi_2, La_2YbGe_2, and Y_2LiSi_2.

(Figure 8d). More importantly, the Bader charge of anionic electrons of the electron-deficient electride Y_2LiSi_2 (−0.13 |e|) is roughly a quarter of those of electron-rich electrides Nd_2ScSi_2 (−0.42 |e|) and La_2YbGe_2 (−0.49 |e|) (Figure 8d). These results prove that the localization degree of anionic electrons is much weaker in the electron-deficient electride than in the electron-rich ones. However, the measured NH_3 synthesis activity of the electron-deficient electride catalyst Ru/Y_2LiSi_2 (~2000 μmol $g_{cat}{}^{-1}$ h^{-1}) is comparable with those of electron-rich catalysts (~1200−3000 μmol $g_{cat}{}^{-1}$ h^{-1}), and it is even higher than that of Ru/La_2YbGe_2 (~1200 μmol $g_{cat}{}^{-1}$ h^{-1}).

Given that the molar masses of the three electrides are quite different (389.61 g mol^{-1} for Nd_2ScSi_2, 596.13 g mol^{-1} for La_2YbGe_2, and 240.92 g mol^{-1} for Y_2LiSi_2), their catalytic activity was renormalized by expressing them per mole (Figure S8) leading to 1169 (1.4%Ru/Nd_2ScSi_2), 745 (1.4%Ru/La_2YbGe_2), and 434 $\mathrm{mmol}_{(NH_3)}\cdot\mathrm{mol}_{cat}{}^{-1}\cdot h^{-1}$ (1.9%Ru/Y_2LiSi_2). This activity is perfectly consistent with the trend of the measured activation energies for these three electride catalysts (Figure S9): 42, 54, and 65 kJ mol^{-1}. The electron-rich electrides thus have a much greater ability to accelerate the reaction process of NH_3 synthesis than their electron-deficient counterparts. Nonetheless, although Y_2LiSi_2 has the lowest catalytic activity per molar amount, its low anionic electron concentration and small molar mass make it a very promising support material for NH_3 synthesis catalysts with high stability.

■ CONCLUSIONS

In this work, a systematic investigation was carried out for screening new A_2BC_2 ternary electrides through a combination of ML and high-throughput DFT calculations. In total, 44 stable and 115 metastable A_2BC_2 electrides, including electron-deficient, electron-neutral, and electron-rich ones, were identified. Among these newly identified electrides, 13 electron-deficient electrides Y_2LiSi_2, Sc_2LiSi_2, La_2LiSi_2, Ce_2LiSi_2, Pr_2LiSi_2, Sm_2LiSi_2, Tb_2LiSi_2, Dy_2LiSi_2, Ho_2LiSi_2, Er_2LiSi_2, Tm_2LiSi_2, Lu_2LiSi_2, and La_2LiGe_2, were found to be thermodynamically metastable phases, i.e., their calculated enthalpies above the convex hull are smaller than 50 meV/atom. ML research in this work not only accelerated the discovery of new electrides but also, by interpreting the feature importance of the trained model, revealed a new mechanism for the formation of electrides. In addition to the electronegativity of cations, the relative polarizability of anions and cations also has an important influence on the formation of electrides in an indirect way.

To validate these predictions, two electron-rich electrides La_2YbGe_2 and Nd_2ScSi_2 were successfully synthesized; moreover, despite the thermodynamical metastability of all identified electron-deficient electrides, Y_2LiSi_2 could also be obtained experimentally. The three compounds were experimentally characterized, displaying typical electride features, e.g., reversible hydrogen storage ability, and low work functions. When loaded with a small amount of Ru, the three electrides show high stability and catalytic activity for NH_3 synthesis. In particular, the electron-deficient electride, Y_2LiSi_2, exhibits a very promising balance between chemical stability and catalytic performance that remains even after washing the sample with water for 5 days. Finally, the electrides found in this work were used as a playground for investigating the correlation between their anionic electron density and catalytic activity. It was demonstrated that the abundance of anionic electrons can greatly promote the catalytic process of the NH_3 synthesis.

This study demonstrates that machine learning can provide useful insights regarding the theoretical study of electrides while being able to effectively screen electrides for a given structural prototype and independent of the charge balance condition. This ML-accelerated work suggests that electrides may not be as rare in the chemical space as one might think and that the electron-deficient electrides are not just fantastical structures only existing in theoretical studies but are real and potentially valuable materials.

EXPERIMENTAL SECTION

First-Principles Calculations. The DFT computations were performed using the Vienna Ab initio Simulation Package (VASP)[77] within the projected augmented wave (PAW) method.[78] The Perdew−Burke−Ernzerhof generalized gradient approximation (PBE-GGA)[79] was adopted for the exchange−correlation potential. The specific pseudopotentials used are those recommended by VASP software (Version 5.4.4). The electronic wave functions were expanded onto a basis set including plane waves up to a cutoff energy of 600 eV. The band structures in the main text were calculated using the PBE+U method. The following U values were adopted for the respective elements: 6.66 eV for Nd, 3.3 eV for Sc, 6.5 eV for La, 8.9 eV for Yb, and 2 eV for Y.[80,81] The Brillouin zone was sampled using Γ-centered $5 \times 5 \times 8$ Monkhorst−Pack k-point grids (k-mesh spacing of 0.03 in units of 2π/Å). The atomic structures were relaxed until the forces on all atoms were lower than 0.02 eV/Å, and the energy did not change by more than 10^{-7} eV.

Electride Synthesis and Characterizations. All of the metals used were purchased from Aladdin Reagent Co., Ltd. La_2YbGe_2 was prepared using a two-step method. First, La granules (99.9%) and Ge pieces (99.9%) were arc-melted with a stoichiometric composition of La:Ge = 1:1 to obtain LaGe intermetallic. The LaGe ingot was ground, mixed with Yb granules (99.9%) with a stoichiometric ratio of 2:1, and then sealed in a stainless-steel crucible filled with Ar. After a continuous heating under 1000 °C for 30 h, La_2YbGe_2 powder was collected and characterized. Nd_2ScSi_2 was prepared with a one-step arc melting route. Nd pieces (99.9%), Sc pieces (99.9%), and Si pieces (99.9%) were mixed by a molar ratio of 2:1:2 and then arc-melted repeatedly five times to ensure homogeneity. The obtained ingot was annealed at 1000 °C for 2 weeks for purification and then crushed and ground in an Ar-filled glovebox before use. The synthesis of Y_2LiSi_2 was carried out following the method previously reported in the literature.[65] The three types of metals, Y, Li, and Si, were thoroughly mixed and annealed at 700 °C for 6 h in a stainless-steel crucible filled with argon (Ar) to produce the Y_2LiSi_2 sample.

Synthesis of Ru-Loaded Catalysts. The Ru-loaded catalysts were prepared via a chemical vapor deposition method, where the desired amount of $Ru_3(CO)_{12}$ was mixed with 0.5 g of the synthesized electride in an Ar-filled glovebox. The mixture was sealed in a quartz tube and then heated with the following program: 1 °C min^{-1} up to 70 °C, hold for 1 h; to 120 °C in 2 h, hold for 1 h; to 250 °C in 2.5 h, hold for 2 h; cooling to ambient temperature. The obtained catalysts were used for performance evaluation and characterizations without further treatment.

Powder X-ray diffraction (XRD) measurements were performed using an X-ray powder diffractometer with a Cu Kα radiation source (Bruker D8 DISCOVER A25). The work functions of the electrides were obtained from UPS measurements (Thermo Scientific ESCALAB 250Xi). UPS spectra were obtained by using a VGS Class150 electron analyzer and discharge lamp that emitted excitation lines of He−I (21.2 eV). For the TPD measurement, hydrogenation of Nd_2ScSi_2 and La_2YbGe_2 powders was performed at 200 °C under a mixed gas flow of 10% H_2 and 90% Ar. Then, the hydrogenated samples were heated from 50 to 800 °C at a rate of 10 °C/min while the TCD signals were recorded. Ru content was evaluated via inductively coupled plasma atomic emission spectroscopy (ICP-AES, Aglient 5110).

Ammonia Synthesis Performance Evaluation. The catalytic performances were evaluated on a fixed bed reactor with a quartz tube reactor (for activity evaluation at 0.1 MPa) or a stainless-steel reactor (for activity evaluations at high pressures). In a typical run, 0.1 g of catalyst was loaded in the reactor and a flow of 60 mL/min (N_2:H_2 = 1:3) was introduced to the reactor. The produced NH_3 was trapped with H_2SO_4 and analyzed by ion chromatography. The reaction activities were calculated based on the NH_3 produced in a certain time interval. The activation energies were calculated based on the Arrhenius equation.

ASSOCIATED CONTENT

Supporting Information

The Supporting Information is available free of charge at https://pubs.acs.org/doi/10.1021/jacs.3c10538.

Algorithm selection and performance of machine learning models; calculated projected band structures and electron localization functions of Y_2LiSi_2, Y_2MgSi_2, Y_2ScSi_2, and Y_2AlSi_2; the variations of ELF_{max} as functions of five features of $\chi(A-B)$, $\chi(B)$, $\alpha(B-C)$, $\alpha(B)$, and $\alpha(A-C)$; band structures; electrostatic (Hartree) potential as a function of the coordinate Z; XRD pattern of Y_2LiSi_2 washed with water for 1 h and 5 days; Arrhenius plot of ammonia synthesis activity on Ru/Y_2LiSi_2; ammonia-synthesis activity per molar amount of different A_2BC_2 compounds with varying Ru loads; Arrhenius plot of ammonia synthesis activity on Ru/La_2YbGe_2; 29 new A_2BC_2 electrides identified from the MP; list of the A_2BC_2 compounds and ELF_{max} used for training the ML model; 28 initial features with their description; the data obtained from the process of feature extraction; and list of the A_2BC_2 electrides with potential magnetic properties (PDF)

AUTHOR INFORMATION

Corresponding Author

Junjie Wang − *State Key Laboratory of Solidification Processing, School of Materials Science and Engineering, Northwestern Polytechnical University, Xi'an, Shaanxi 710072, People's Republic of China;* orcid.org/0000-0002-6428-2233; Email: wang.junjie@nwpu.edu.cn

Authors

Zhiqi Wang − *State Key Laboratory of Solidification Processing, School of Materials Science and Engineering, Northwestern Polytechnical University, Xi'an, Shaanxi 710072, People's Republic of China*

Yutong Gong − *State Key Laboratory of Solidification Processing, School of Materials Science and Engineering, Northwestern Polytechnical University, Xi'an, Shaanxi 710072, People's Republic of China;* orcid.org/0000-0003-4676-9547

Matthew L. Evans − *IMCN-MODL, Université Catholique de Louvain, Louvain-la-Neuve B-1348, Belgium*

Yujing Yan − *State Key Laboratory of Solidification Processing, School of Materials Science and Engineering, Northwestern Polytechnical University, Xi'an, Shaanxi 710072, People's Republic of China*

Shiyao Wang − *State Key Laboratory of Solidification Processing, School of Materials Science and Engineering, Northwestern Polytechnical University, Xi'an, Shaanxi 710072, People's Republic of China*

Nanxi Miao − *State Key Laboratory of Solidification Processing, School of Materials Science and Engineering, Northwestern Polytechnical University, Xi'an, Shaanxi 710072, People's Republic of China*

Ruiheng Zheng − *State Key Laboratory of Solidification Processing, School of Materials Science and Engineering, Northwestern Polytechnical University, Xi'an, Shaanxi 710072, People's Republic of China*

Gian-Marco Rignanese − *State Key Laboratory of Solidification Processing, School of Materials Science and Engineering, Northwestern Polytechnical University, Xi'an,* *Shaanxi 710072, People's Republic of China; IMCN-MODL, Université Catholique de Louvain, Louvain-la-Neuve B-1348, Belgium;* orcid.org/0000-0002-1422-1205

Complete contact information is available at:
https://pubs.acs.org/10.1021/jacs.3c10538

Notes

The authors declare no competing financial interest.

■ ACKNOWLEDGMENTS

This work is supported by the National Natural Science Foundation of China (Grant No. 52272307), the National Key Research and Development Program of Intergovernmental Cooperation in Science and Technology (Grant No. 2022YFE0141100), the Fundamental Research Funds for the Central Universities (No. D5000220172), the China Postdoctoral Science Foundation (No. 2021M692634), and the Innovation Foundation for Doctor Dissertation of Northwestern Polytechnical University (Grants No. CX2021063). M.L.E. thanks the BEWARE scheme of the Wallonia-Brussels Federation for funding under the European Commission's Marie Curie-Skłodowska Action (COFUND 847587).

■ REFERENCES

(1) Hosono, H.; Kitano, M. Advances in Materials and Applications of Inorganic electrides. *Chem. Rev.* **2021**, *121*, 3121−3185.

(2) Matsuishi, S.; Toda, Y.; Miyakawa, M.; Hayashi, K.; Kamiya, T.; Hirano, M.; Tanaka, I.; Hosono, H. High-density electron anions in a nanoporous single crystal: $[Ca_{24}Al_{28}O_{64}]^{4+}(4e^-)$. *Science* **2003**, *301*, 626−629.

(3) Dye, J. L. electrides: Early Examples of Quantum Confinement. *Acc. Chem. Res.* **2009**, *4*, 1564−1572.

(4) Kim, K. B.; Kikuchi, M.; Miyakawa, M.; Yanagi, H.; Kamiya, T.; Hirano, M.; Hosono, H. Photoelectron spectroscopic study of C12A7:e^- and Alq_3 interface: The formation of a low electron-injection barrier. *J. Phys. Chem. C* **2007**, *111*, 8403−8406.

(5) Miyakawa, M.; Kim, S. W.; Hirano, M.; Kohama, Y.; Kawaji, H.; Atake, T.; Ikegami, H.; Kono, K.; Hosono, H. Superconductivity in an inorganic electride $12CaO\cdot7Al_2O_3:e^-$. *J. Am. Chem. Soc.* **2007**, *129*, 7270−7271.

(6) Hu, J.; Xu, B.; Yang, S. A.; Guan, S.; Ouyang, C.; Yao, Y. 2D electrides as Promising Anode Materials for Na-Ion Batteries from First-Principles Study. *ACS Appl. Mater. Interfaces* **2015**, *7*, 24016−24022.

(7) Kitano, M.; Inoue, Y.; Yamazaki, Y.; Hayashi, F.; Kanbara, S.; Matsuishi, S.; Yokoyama, T.; Kim, S. W.; Hara, M.; Hosono, H. Ammonia synthesis using a stable electride as an electron donor and reversible hydrogen store. *Nat. Chem.* **2012**, *4*, 934−940.

(8) Kitano, M.; Kanbara, S.; Inoue, Y.; Kuganathan, N.; Sushko, P. V.; Yokoyama, T.; Hara, M.; Hosono, H. electride support boosts nitrogen dissociation over ruthenium catalyst and shifts the bottleneck in ammonia synthesis. *Nat. Commun.* **2015**, *6*, 6731.

(9) Wu, J.; Li, J.; Gong, Y.; Kitano, M.; Inoshita, T.; Hosono, H. Intermetallic electride Catalyst as a Platform for Ammonia Synthesis. *Angew. Chem., Int. Ed.* **2019**, *58*, 825−829.

(10) Zhang, X.; Xiao, Z.; Lei, H.; Toda, Y.; Matsuishi, S.; Kamiya, T.; Ueda, S.; Hosono, H. Two-Dimensional Transition-Metal electride Y_2C. *Chem. Mater.* **2014**, *26*, 6638−6643.

(11) Lu, Y.; Li, J.; Tada, T.; Toda, Y.; Ueda, S.; Yokoyama, T.; Kitano, M.; Hosono, H. Water Durable electride Y_5Si_3: Electronic Structure and Catalytic Activity for Ammonia Synthesis. *J. Am. Chem. Soc.* **2016**, *138*, 3970−3973.

(12) Wu, J.; Gong, Y.; Inoshita, T.; Fredrickson, D. C.; Wang, J.; Lu, Y.; Kitano, M.; Hosono, H. Tiered Electron Anions in Multiple Voids of LaScSi and Their Applications to Ammonia Synthesis. *Adv. Mater.* **2017**, *29*, 1700924.

(13) McRae, L. M.; Radomsky, R. C.; Pawlik, J. T.; Druffel, D. L.; Sundberg, J. D.; Lanetti, M. G.; Donley, C. L.; White, K. L.; Warren, S. C. Sc_2C, a 2D Semiconducting electride. *J. Am. Chem. Soc.* **2022**, *144*, 10862−10869.

(14) Lu, Y.; Wang, J.; Li, J.; Wu, J.; Kanno, S.; Tada, T.; Hosono, H. Realization of Mott-insulating electrides in dimorphic Yb_5Sb_3. *Phys. Rev. B* **2018**, *98*, No. 125128.

(15) Wang, J.; Hanzawa, K.; Hiramatsu, H.; Kim, J.; Umezawa, N.; Iwanaka, K.; Tada, T.; Hosono, H. Exploration of Stable Strontium Phosphide-Based electrides: Theoretical Structure Prediction and Experimental Validation. *J. Am. Chem. Soc.* **2017**, *139*, 15668−15680.

(16) Inoshita, T.; Jeong, S.; Hamada, N.; Hosono, H. Exploration for Two-Dimensional electrides via Database Screening and Ab Initio Calculation. *Phys. Rev. X* **2014**, *4*, No. 031023.

(17) Wang, J.; Zhu, Q.; Wang, Z.; Hosono, H. Ternary inorganic electrides with mixed bonding. *Phys. Rev. B* **2019**, *99*, No. 064104.

(18) Zhu, Q.; Frolov, T.; Choudhary, K. Computational Discovery of Inorganic electrides from an Automated Screening. *Matter* **2019**, *1*, 1293−1303.

(19) Zhou, J.; Shen, L.; Yang, M.; Cheng, H.; Kong, W.; Feng, Y. P. Discovery of Hidden Classes of Layered electrides by Extensive High-Throughput Material Screening. *Chem. Mater.* **2019**, *31*, 1860−1868.

(20) Burton, L. A.; Ricci, F.; Chen, W.; Rignanese, G. M.; Hautier, G. High-Throughput Identification of electrides from All Known Inorganic Materials. *Chem. Mater.* **2018**, *30*, 7521−7526.

(21) Dale, S. G.; Johnson, E. R. Theoretical Descriptors of electrides. *J. Phys. Chem. A* **2018**, *122*, 9371−9391.

(22) Walsh, A.; Scanlon, D. O. Electron excess in alkaline earth subnitrides: 2D electron gas or 3D electride? *J. Mater. Chem. C* **2013**, *1*, 3525−3528.

(23) Kulichenko, M.; Fedik, N.; Bozhenko, K. V.; Boldyrev, A. I. Inorganic Molecular electride Mg_4O_3: Structure, Bonding, and Nonlinear Optical Properties. *Chem.—Eur. J.* **2019**, *25*, 5311−5315.

(24) Ma, Y.; Eremets, M.; Oganov, A. R.; Xie, Y.; Trojan, I.; Medvedev, S.; Lyakhov, A. O.; Valle, M.; Prakapenka, V. Transparent dense sodium. *Nature* **2009**, *458*, 182−185.

(25) Cheng, W.; Li, K.; Tada, T.; Hosono, H.; Wang, J. electride Formation in Ba-P System and the Unexpected Structure Transition of electrides under Pressure. *J. Phys. Chem. C* **2022**, *126*, 16815−16824.

(26) Li, K.; Wang, J.; Oganov, A. R. High-Pressure Phase Diagram of the Ti-O System. *J. Phys. Chem. Lett.* **2021**, *12*, 5486−5493.

(27) Gong, Y.; Li, H.; Li, C.; Yang, X.; Wang, J.; Hosono, H. LaRuSi electride Disrupts the Scaling Relations for Ammonia Synthesis. *Chem. Mater.* **2022**, *34*, 1677−1685.

(28) Li, K.; Gong, Y.; Wang, J.; Hosono, H. Electron-Deficient-Type electride Ca_5Pb_3: Extension of electride Chemical Space. *J. Am. Chem. Soc.* **2021**, *143*, 8821−8828.

(29) Li, K.; Blatov, V. A.; Wang, J. Discovery of electrides in Electron-Rich Non-electride Materials via Energy Modification of Interstitial Electrons. *Adv. Funct. Mater.* **2022**, *32*, 2112198.

(30) Long, T.; Fortunato, N. M.; Opahle, I.; Zhang, Y.; Samathrakis, I.; Shen, C.; Gutfleisch, O.; Zhang, H. Constrained crystals deep convolutional generative adversarial network for the inverse design of crystal structures. *NPJ Comput. Mater.* **2021**, *7*, 66.

(31) Ryan, K.; Lengyel, J.; Shatruk, M. Crystal Structure Prediction via Deep Learning. *J. Am. Chem. Soc.* **2018**, *140*, 10158−10168.

(32) Kim, B.; Lee, S.; Kim, J. Inverse design of porous materials using artificial neural networks. *Sci. Adv.* **2020**, *6*, No. eaax9324.

(33) Schneider, E.; Dai, L.; Topper, R. Q.; Drechsel-Grau, C.; Tuckerman, M. E. Stochastic Neural Network Approach for Learning High-Dimensional Free Energy Surfaces. *Phys. Rev. Lett.* **2017**, *119*, No. 150601.

(34) Behler, J. First Principles Neural Network Potentials for Reactive Simulations of Large Molecular and Condensed Systems. *Angew. Chem., Int. Ed. Engl.* **2017**, *56*, 12828−12840.

(35) Sun, X.; Zheng, J.; Gao, Y.; Qiu, C.; Yan, Y.; Yao, Z.; Deng, S.; Wang, J. Machine-learning-accelerated screening of hydrogen

evolution catalysts in MBenes materials. *Appl. Surf. Sci.* **2020**, *526*, No. 146522.

(36) Ma, S.; Liu, Z. P. Machine Learning for Atomic Simulation and Activity Prediction in Heterogeneous Catalysis: Current Status and Future. *ACS Catal.* **2020**, *10*, 13213−13226.

(37) Wexler, R. B.; Martirez, J. M. P.; Rappe, A. M. Chemical Pressure-Driven Enhancement of the Hydrogen Evolving Activity of Ni_2P from Nonmetal Surface Doping Interpreted via Machine Learning. *J. Am. Chem. Soc.* **2018**, *140*, 4678−4683.

(38) Wang, H. C.; Botti, S.; Marques, M. A. L. Predicting stable crystalline compounds using chemical similarity. *NPJ Comput. Mater.* **2021**, *7*, 12.

(39) Tao, Q.; Xu, P.; Li, M.; Lu, W. Machine learning for perovskite materials design and discovery. *NPJ Comput. Mater.* **2021**, *7*, 23.

(40) Im, J.; Lee, S.; Ko, T. W.; Kim, H. W.; Hyon, Y.; Chang, H. Identifying Pb-free perovskites for solar cells by machine learning. *NPJ Comput. Mater.* **2019**, *5*, 37.

(41) Lu, S.; Zhou, Q.; Ouyang, Y.; Guo, Y.; Li, Q.; Wang, J. Accelerated discovery of stable lead-free hybrid organic-inorganic perovskites via machine learning. *Nat. Commun.* **2018**, *9*, 3405.

(42) Pilania, G.; Wang, C.; Jiang, X.; Rajasekaran, S.; Ramprasad, R. Accelerating materials property predictions using machine learning. *Sci. Rep.* **2013**, *3*, 2810.

(43) Iwasaki, Y.; Sawada, R.; Stanev, V.; Ishida, M.; Kirihara, A.; Omori, Y.; Someya, H.; Takeuchi, I.; Saitoh, E.; Yorozu, S. Identification of advanced spin-driven thermoelectric materials via inter-pretable machine learning. *NPJ Comput. Mater.* **2019**, *5*, 6.

(44) Ryu, B.; Wang, L.; Pu, H.; Chan, M. K. Y.; Chen, J. Understanding, discovery, and synthesis of 2D materials enabled by machine learning. *Chem. Soc. Rev.* **2022**, *51*, 1899−1925.

(45) Oh, S. V.; Hwang, W.; Kim, K.; Lee, J. H.; Soon, A. Using Feature-Assisted Machine Learning Algorithms to Boost Polarity in Lead-Free Multicomponent Niobate Alloys for High-Performance Ferroelectrics. *Adv. Sci.* **2022**, *9*, No. e2104569.

(46) Jain, A.; Ong, S. P.; Hautier, G.; Chen, W.; Richards, W. D.; Dacek, S.; Cholia, S.; Gunter, D.; Skinner, D.; Ceder, G.; Persson, K. A. Commentary: The Materials Project: A materials genome approach to accelerating materials innovation. *APL Mater.* **2013**, *1*, No. 011002.

(47) Becke, A. D.; Edgecombe, K. E. A simple measure of electron localization in atomic and molecular systems. *J. Chem. Phys.* **1990**, *9*, 5397−5403.

(48) Li, Z. Y.; Yang, J. L.; Hou, J. G.; Zhu, Q. S. Is mayenite without clathrated oxygen an inorganic electride? *Angew. Chem., Int. Ed.* **2004**, *43*, 6479−6482.

(49) Zheng, Q.; Feng, T.; Hachtel, J. A.; Ishikawa, R.; Cheng, Y.; Daemen, L.; Xing, J.; Idrobo, J. C.; Yan, J.; Shibata, N.; Ikuhara, Y.; Sales, B. C.; Pantelides, S. T.; Chi, M. Direct visualization of anionic electrons in an electride reveals inhomogeneities. *Sci. Adv.* **2021**, *7*, No. eabe6819.

(50) Zhang, Y.; Wang, H.; Wang, Y.; Zhang, L.; Ma, Y. Computer-Assisted Inverse Design of Inorganic electrides. *Phys. Rev. X* **2017**, *7*, No. 011017.

(51) Savin, A. The electron localization function (ELF) and its relatives: interpretations and difficulties. *J. Mol. Struc-Theochem.* **2005**, *727*, 127−131.

(52) Vidal, I.; Melchor, S.; Dobado, J. A. On the nature of metal-carbon bonding: AIM and ELF analyses of MCH(n) (n = 1−3) compounds containing early transition metals. *J. Phys. Chem. A* **2005**, *109*, 7500−7508.

(53) Everitt, B. S. *Encyclopedia of Statistics in Behavioral Science*. John Wiley & Sons: New York, 2005 2 878 DOI: 10.1002/0470013192.

(54) Freund, Y.; Schapire, R. E. A Decision-Theoretic Generalization of On-Line Learning and an Application to Boosting. *J. Comput. Syst. Sci.* **1997**, *55*, 119−139.

(55) Chen, T.; Guestrin, C., XGBoost: A Scalable Tree Boosting System. In *Proceedings of the 22nd ACM SIGKDD International Conference on Knowledge Discovery and Data Mining*, 2016, 785−794 DOI: 10.1145/2939672.2939785.

(56) Vapnik, V. N. *The Nature of Statistical Learning Theory*. Springer: New York, 1995 DOI: 10.1007/978-1-4757-2440-0).

(57) Friedman, J. H. Greedy Function Approximation: A Gradient Boosting Machine. *Ann. Stat.* **2001**, *29*, 1189−1232.

(58) Ong, S. P.; Richards, W. D.; Jain, A.; Hautier, G.; Kocher, M.; Cholia, S.; Gunter, D.; Chevrier, V. L.; Persson, K. A.; Ceder, G. Python Materials Genomics (pymatgen): A robust, open-source python library for materials analysis. *Comput. Mater. Sci.* **2013**, *68*, 314−319.

(59) Sun, W.; Dacek, S. T.; Ong, S. P.; Hautier, G.; Jain, A.; Richards, W. D.; Gamst, A. C.; Persson, K. A.; Ceder, G. The thermodynamic scale of inorganic crystalline metastability. *Sci. Adv.* **2016**, *2*, No. e1600225.

(60) Talirz, L.; Kumbhar, S.; Passaro, E.; Yakutovich, A. V.; Granata, V.; Gargiulo, F.; Borelli, M.; Uhrin, M.; Huber, S. P.; Zoupanos, S.; Adorf, C. S.; Andersen, C. W.; Schütt, O.; Pignedoli, C. A.; Passerone, D.; VandeVondele, J.; Schulthess, T. C.; Smit, B.; Pizzi, G.; Marzari, N. Materials Cloud, a platform for open computational science. *Sci. Data* **2020**, *7* (1), 299.

(61) Andersen, C. W.; Armiento, R.; Blokhin, E.; Conduit, G. J.; Dwaraknath, S.; Evans, M. L.; Fekete, Á.; Gopakumar, A.; Gražulis, S.; Merkys, A.; Mohamed, F.; Oses, C.; Pizzi, G.; Rignanese, G.-M.; Scheidgen, M.; Talirz, L.; Toher, C.; Winston, D.; Aversa, R.; Choudhary, K.; Colinet, P.; Curtarolo, S.; Di Stefano, D.; Draxl, C.; Er, S.; Esters, M.; Fornari, M.; Giantomassi, M.; Govoni, M.; Hautier, G.; Hegde, V.; Horton, M. K.; Huck, P.; Huhs, G.; Hummelshøj, J.; Kariryaa, A.; Kozinsky, B.; Kumbhar, S.; Liu, M.; Marzari, N.; Morris, A. J.; Mostofi, A. A.; Persson, K. A.; Petretto, G.; Purcell, T.; Ricci, F.; Rose, F.; Scheffler, M.; Speckhard, D.; Uhrin, M.; Vaitkus, A.; Villars, P.; Waroquiers, D.; Wolverton, C.; Wu, M.; Yang, X. OPTIMADE, an API for exchanging materials data. *Sci. Data* **2021**, *8* (1), 217.

(62) Evans, M.; Andersen, C.; Dwaraknath, S.; Scheidgen, M.; Fekete, Á.; Winston, D. OPTIMADE-python-tools: a Python library for serving and consuming materials data via OPTIMADE APIs. *JOSS.* **2021**, *6*, 3458.

(63) Mizoguchi, H.; Park, S. W.; Katase, T.; Vazhenin, G. V.; Kim, J.; Hosono, H. Origin of Metallic Nature of Na_3N. *J. Am. Chem. Soc.* **2021**, *143*, 69−72.

(64) Qu, J.; Zhu, S.; Zhang, W.; Zhu, Q. electrides with Dinitrogen Ligands. *ACS Appl. Mater. Interfaces* **2019**, *11*, 5256−5263.

(65) Honda, F.; Yoshitani, N.; Hirose, Y.; Ishida, K.; Maeta, T.; Miyake, A.; Tanaka, S.; Shimizu, K.; Takeuchi, T.; Matsubayashi, K.; Uwatoko, Y.; Settai, R.; Aoki, D.; Ōnuki, Y. Drastic Change of Electronic Properties in Ce_2MgSi_2 and $CeNiIn_4$ under High Pressure. *JPS Conf. Proc.* **2014**, *3*, No. 012026.

(66) Banakh, O. E.; Kotur, B. Y. The Sc−Nd−Si ternary system at 870 K. *J. Alloys Compd.* **1998**, *268*, L3−L5.

(67) Steinberg, G.; Schuster, H. U. Ternary Silieides of Lithium with Yttrium or Neodymium in a Modified U_3Si_2-Type Structure. *Z. Naturforsch. B* **1979**, *34*, 1237−1239.

(68) Jiang, Y.; Takashima, R.; Nakao, T.; Miyazaki, M.; Lu, Y.; Sasase, M.; Niwa, Y.; Abe, H.; Kitano, M.; Hosono, H. Boosted Activity of Cobalt Catalysts for Ammonia Synthesis with $BaAl_2O_{4-x}H_y$ electrides. *J. Am. Chem. Soc.* **2023**, *145*, 10669−10680.

(69) Cao, Y.; Toshcheva, E.; Almaksoud, W.; Ahmad, R.; Tsumori, T.; Rai, R.; Tang, Y.; Cavallo, L.; Kageyama, H.; Kobayashi, Y. Ammonia Synthesis via an Associative Mechanism on Alkaline Earth Metal Sites of Ca_3CrN_3H. *ChemSusChem* **2023**, No. e202300234.

(70) Gong, Y.; Wu, J.; Kitano, M.; Wang, J.; Ye, T. N.; Li, J.; Kobayashi, Y.; Kishida, K.; Abe, H.; Niwa, Y.; Yang, H.; Tada, T.; Hosono, H. Ternary intermetallic LaCoSi as a catalyst for N_2 activation. *Nat. Catal.* **2018**, *1*, 178−185.

(71) Gong, Y.; Li, H.; Li, C.; Bao, X.; Hosono, H.; Wang, J. Insight into rare-earth-incorporated catalysts: The chance for a more efficient ammonia synthesis. *J. Adv. Ceram.* **2022**, *11*, 1499−1529.

(72) Kitano, M.; Inoue, Y.; Ishikawa, H.; Yamagata, K.; Nakao, T.; Tada, T.; Matsuishi, S.; Yokoyama, T.; Hara, M.; Hosono, H. Essential role of hydride ion in ruthenium-based ammonia synthesis catalysts. *Chem. Sci.* **2016**, *7*, 4036−4043.

(73) Mizoguchi, H.; Okunaka, M.; Kitano, M.; Matsuishi, S.; Yokoyama, T.; Hosono, H. Hydride-Based electride Material, LnH_2 (Ln = La, Ce, or Y). *Inorg. Chem.* **2016**, *55*, 8833−8838.

(74) Lee, K.; Kim, S. W.; Toda, Y.; Matsuishi, S.; Hosono, H. Dicalcium nitride as a two-dimensional electride with an anionic electron layer. *Nature.* **2013**, *494*, 336−340.

(75) Feng, J.; Liu, L.; Zhang, X.; Wang, J.; Ju, X.; Li, R.; Guo, J.; He, T.; Chen, P. Ru nanoparticles on Y_2O_3 with enhanced metal−support interactions for efficient ammonia synthesis. *Catal. Sci. Technol.* **2023**, *13*, 844−853.

(76) Kanbara, S.; Kitano, M.; Inoue, Y.; Yokoyama, T.; Hara, M.; Hosono, H. Mechanism Switching of Ammonia Synthesis Over Ru-Loaded electride Catalyst at Metal-Insulator Transition. *J. Am. Chem. Soc.* **2015**, *137*, 14517−14524.

(77) Kresse, G.; Furthmüller, J. Efficiency of ab-initio total energy calculations for metals and semiconductors using a plane-wave basis set. *Comput. Mater. Sci.* **1996**, *6*, 15−50.

(78) Kresse, G.; Joubert, D. From ultrasoft pseudopotentials to the projector augmented-wave method. *Phys. Rev. B* **1999**, *59*, 1758−1775.

(79) Perdew, J. P.; Burke, K.; Ernzerhof, M. Generalized Gradient Approximation Made Simple. *Phys. Rev. Lett.* **1998**, *77*, 3865−3868.

(80) Larson, P.; Lambrecht, W. R. L.; Chantis, A.; van Schilfgaarde, M. Electronic structure of rare-earth nitrides using the LSDA+U approach: Importance of allowing 4*f* orbitals to break the cubic crystal symmetry. *Phys. Rev. B* **2007**, *75* (4), No. 045114.

(81) Kirchner-Hall, N. E.; Zhao, W.; Xiong, Y.; Timrov, I.; Dabo, I. Extensive Benchmarking of DFT+U Calculations for Predicting Band Gaps. *Appl. Sci.* **2021**, *11*, 2395.